Supplementary Material

CRESCENT-1D: A 1D solver of coupled charge and light transport in heterostructures for the design of near-field thermophotonic engines

Julien Legendre, Pierre-Olivier Chapuis

CONTENTS

S.I. NEAR-FIELD RADIATIVE HEAT TRANSFER BETWEEN ARBITRARILY CLOSE BODIES

To highlight the issues encountered with the near-field radiation model when the distance separating the emission and absorption location, we consider here a simple system, for which the near-field transmission coefficient can be expressed analytically. This system is composed by three slabs (numbered 1 to 3) placed between two semi-infinite media (numbered 0 and 4). All layers are made of the same lossy material, and we focus on the transmission coefficient between slabs 1 and 3 (see Fig. S1a) which can be expressed as [1], [2]

$$\mathcal{T}_{13}^{\gamma}(\omega, k_\rho) = \frac{1}{|k_{z1}|^2}\kappa_1^{\gamma}\kappa_3^{\gamma}|t_2^{\gamma}|^2\vartheta_1\vartheta_3, \tag{S1}$$

γ being the polarisation (TE or TM), k_{z1} is the perpendicular component of the wavevector in medium 1, and t_2^{γ} is the transmission coefficient through slab 2. κ_i^{γ} is an effective wavenumber in layer i, which respectively equals $\mathrm{Re}(k_{zi})$ for TE and $\mathrm{Re}(\varepsilon_{ri}k_{zi}^*)/|\varepsilon_{ri}|$ for TM polarisation. At last, $\vartheta_i = 1 - e^{-2\mathrm{Im}(k_{zi})t_i}$ is a factor that accounts for the limited thickness t_i of layer i.

The transmission coefficient obtained between 1 nm thick slabs at a photon energy of 1.42 eV and for a dielectric function $\epsilon = 10 + i$ is depicted in Figure S1b. For both

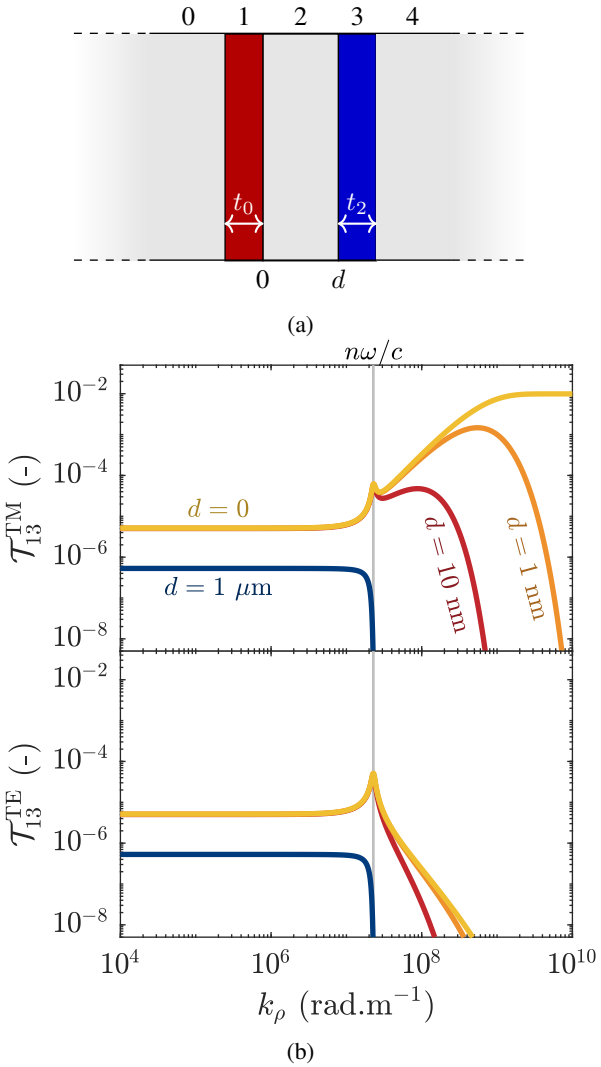

Fig. S1: (a) Schematic of the system considered to highlight radiative heat transfer divergence for vanishing gap distance. (b) Variations of the photon transmission coefficient with k_ρ obtained for various separation distances.

J. Legendre was with Univ Lyon, CNRS, INSA-Lyon, Université Claude Bernard Lyon 1, CETHIL UMR5008, F-69621, Villeurbanne, France. He is now with ICFO-Institut de Ciencies Fotoniques, Barcelona, Spain (e-mail: julien.legendre@icfo.eu).

P.-O. Chapuis is with Univ Lyon, CNRS, INSA-Lyon, Université Claude Bernard Lyon 1, CETHIL UMR5008, F-69621, Villeurbanne, France (e-mail: pierre-olivier.chapuis@insa-lyon.fr).

polarisations, decreasing the gap distance leads to an increase in the transmission coefficient for propagating modes - especially close to $k_\rho = n\omega/c$ - and gives rise to the transmission of photons through evanescent modes. But while the TE transmission coefficient goes to zero as $k_\rho \to \infty$ for d approaching 0, it goes to a constant non-zero value in the case of TM modes. Consequently, the monochromatic heat flux obtained after integration over k_ρ converges for TE modes as $d \to 0$, but diverges for TM modes.

Such a divergence is caused by the absence of non-local effect (i.e., spatial dispersion) at small scale [3]. In the present work, as in most of the literature on near-field radiation, we have assumed optical properties to be local, i.e. that the movement of dipoles at a given position has no impact at any other position at the same time. While correct in most cases, this hypothesis definitely breaks down when the gap distance goes below the nanometre, and may have a significant impact at larger distances. To take non-local effects into account, the dielectric function must be modified to include dependence on k_ρ [3]. [4] also proposed to replace the Dirac function $\delta(\mathbf{r}'-\mathbf{r}'')$ in the fluctuation-dissipation theorem by a Gaussian function depending on a local distance l. While being a promising solution due to its simplicity, some discrepancies were found in our implementation of the article, with some expressions that may lead to non-zero heat flux between two media at the same temperature for instance. Additional work would thus be required. We note that works dealing with heat conduction by radiative modes performed the k_ρ-integration up to $n\omega/c$ only [5].

S.II. Material properties

We provide in Table I the source of the various material properties used for InGaAs and InGaP. Because of the lack of accurate data, only the bandgap energy, the interband contribution to the dielectric function and the charge carrier mobility are temperature-dependent quantities. The other ones are taken at room temperature. The interband contribution given in [6] lacks composition and temperature dependence, but these are included by gathering the variations of E_g with x and T from the literature; we then assume that each transition energy $E_0 = E_g$, E_1 and E_2 varies as E_g. For the temperature dependence, we consider the linear variation given in [7]. The composition-dependent bandgap is obtained from a second-order polynomial fit from the data at $x_{\mathrm{Ga}} = 0$ ($E_g = 1.34$ eV [8]), $x_{\mathrm{Ga}} = 0.51$ ($E_g = 1.89$ eV [6]) and $x_{\mathrm{Ga}} = 0.71$ ($E_g = 2.2$ eV [9]). Similarly, the composition dependence of the phonon contribution in InGaAs is modelled using linear interpolation between GaAs [10] and InAs [11] data.

We do not take into account the composition dependence of the phonon contribution in InGaP, nor that of the non-radiative recombination coefficients of both InGaAs and InGaP. In fact, for InGaP, no accurate data was found for the SRH lifetime, and we have therefore used that of GaAs - this should only bring a limited error in the final result since most of the recombinations occur in the InGaAs active layers. As shown in [16], including temperature and composition dependence of these coefficients in (at least) InGaAs will be essential to correctly estimate the performance of TPX devices.

TABLE I: Material properties used for $\mathrm{In}_x\mathrm{Ga}_{1-x}\mathrm{As}$ and $\mathrm{In}_x\mathrm{Ga}_{1-x}\mathrm{P}$ alloys.

Parameter	Symbol	InGaAs	InGaP
High freq. dielectric cst.	ε_∞	[10], [11]	[8]
Static dielectric cst	ε_{rs}	[8]	[8]
Dielectric function	ε_r		
Phonon contrib. (Lorentz)		[10], [11]	[12]
Interband contribution		[13]	[6]
Lattice constant	a	[8]	[8]
Bandgap energy	E_g	[13]	[6]
Electron affinity	χ	[8]	[8]
Electron/hole effective mass	$m^*_{n/p}$	[8]	[8]
Electron/hole mobility	μ	[14]	[14]
SRH lifetime	$\tau_{n/p,\mathrm{SRH}}$	[15]	[15]
Auger rec. coefficient	$C_{n/p}$	[15]	[8]

Although plasmon contribution to the dielectric function is not mentioned in Table I, it is included in the solver using the classical Drude model

$$\varepsilon_r = \varepsilon_\infty \left(1 - \frac{\omega_\mathrm{p}^2}{\omega(\omega + i\Gamma)}\right), \tag{S2}$$

where the plasmon frequency ω_p and the damping coefficient Γ are expressed as

$$\omega_\mathrm{p} = \sqrt{\frac{Ne^2}{m^*\varepsilon_\infty\varepsilon_0}}, \tag{S3a}$$

$$\Gamma = \frac{e}{m^*\mu}. \tag{S3b}$$

For simplicity, in each layer, we only consider the plasmon contribution related to the carriers corresponding to the doping type, and the charge carrier density N is approximated by the doping level.

Finally, we should mention that only rough estimation of the lattice constant given in [8] has been considered for ease: $a(\text{Å}) = 5.7 + 0.4x$ for InGaAs, and $a(\text{Å}) = 5.9 - 0.4x$ for InGaP.

S.III. Details on the thermionic emission and charge carrier tunnelling model

In CRESCENT-1D, only abrupt heterojunctions are considered. The presence of potential barriers at such junctions causes the transmission probability of charge carriers from one side to the other to be asymmetric, eventually giving rise to a discontinuity in the quasi-Fermi levels. To express the relation between the current flow perpendicular to heterointerfaces (z-direction) and the quasi-Fermi levels, one can start with the general expression for the net current density of charge carrier c between layers i and j [17], [18]:

$$J_c = A^- T^2 \iint \mathcal{T}(\tilde{E}) \left(f^+(\tilde{E}) - f^-(\tilde{E})\right) d\tilde{E}_\rho^- d\tilde{E}_z^-, \tag{S4}$$

where A^- represents the effective Richardson constant in the layer placed before the interface, and equals $em_c^{*,-}k_\mathrm{B}^2/2\pi^2\hbar^3$. $\mathcal{T}$ represents here the transmission coefficient of charge carriers and f their distribution function. $\tilde{E} = E/k_\mathrm{B}T$ is the normalised energy of the carrier, and is conserved through

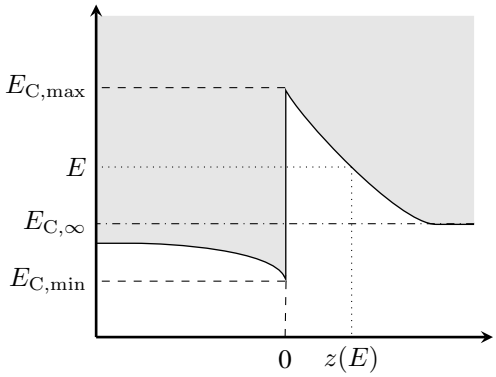

Fig. S2: Representation of the different quantities useful for modelling charge carrier tunnelling.

the interface: $E^- = E^+$. Taking the example of electrons in the conduction band, this energy can be decomposed as $E^- = (E_\rho^- + E_z^-) + E_\mathrm{C}^-$, E_ρ and E_z representing respectively the kinetic energy in the direction parallel and perpendicular to the interface and being equal to $\hbar^2 k_\rho^2 / 2m_n^*$ and $\hbar^2 k_z^2 / 2m_n^*$.

We first consider thermionic emission. Then, $\mathcal{T}(\tilde{E})$ is equal to one only if $\tilde{E}$ is larger than $\tilde{E}_{\mathrm{C,max}}$; else, it equals zero. To determine the domain of integration for $\tilde{E}_\rho^-$ and $\tilde{E}_z^-$, we only consider what happens at the interface, as in [17] and contrarily to [18] in which the maximum of the conduction band is not forced to be at the interface. We can then make use of several equations:

- the conservation of momentum parallel to the interface $m_c^{*,-}\tilde{E}_\rho^- = m_c^{*,+}\tilde{E}_\rho^+$;
- the conservation of energy $\tilde{E}^- = \tilde{E}^+$;
- the condition that every kinetic term should be positive.

From these, we obtain that the integration on $E_{z,i}$ should be carried from $\alpha = \max(E_\mathrm{B}, 0)$ to infinity, where E_B represents the barrier height (e.g. equal to $E_\mathrm{C}^+ - E_\mathrm{C}^-$ for electrons). For the integration on $E_{\rho,i}$, it must be computed from 0 to a parameter $\beta(E_{z,i})$ which depends on the ratio $\theta = m_c^{*,+}/m_c^{*,-}$: $\beta = \infty$ for $\theta \geq 1$, but $\beta = (E_z^- - E_\mathrm{B})/(1/\theta - 1)$ else. Using Boltzmann's approximation to simplify the Fermi-Dirac distribution of charge carriers, the integration is straightforward. Considering electrons once more (a similar result can be obtained for holes), it leads to

$$J_{n,\mathrm{thermionic}} = AT^2 \eta_n e^{-\tilde{E}_{\mathrm{C,max}}} (\Phi_n^+ - \Phi_n^-), \qquad \text{(S5)}$$

where A is the free electron Richardson constant. η_n includes the effects related to effective mass asymmetry and is expressed as

$$\eta_n = \frac{m_{\mathrm{min}}^*}{m_0} + \frac{\Delta m^*}{m_0}\left(1 - \exp\left(-\frac{m_{\mathrm{min}}^*}{\Delta m^*}\max(\Delta\tilde{E}_\mathrm{C}, 0)\right)\right), \qquad \text{(S6)}$$

where m_0 is the free electron mass, $\Delta m^* = m_{\mathrm{max}}^* - m_{\mathrm{min}}^*$ and $\Delta\tilde{E}_\mathrm{C} = \tilde{E}_{\mathrm{C},m_{\mathrm{max}}^*} - \tilde{E}_{\mathrm{C},m_{\mathrm{min}}^*}$. In SCAPS, η_n is supposed to be equal to m_{min}^* [19]: we see here that this approximation, although being mostly correct, fails when $\Delta\tilde{E}_\mathrm{C} \gg 0$ as η_n moves from m_{min}^* to m_{max}^*.

We now move on to the modelling of charge carrier tunnelling, i.e. to the quantum transport of charges through a normally forbidden region. In CRESCENT-1D, only intraband tunnelling is included, meaning that charges that are tunnelling remain in the same band. The current at the heterojunction can be once more obtained from Eq. (S4), however with different integration bounds. Integration can be done separately for classical and quantum transmission, so that the current can be expressed as the sum of the two contributions. In the following, we take once more the example of electrons in the conduction band, the development being similar for holes in the valence band. In order to compute J_{tunnel} at a position z, the integral over energy should only be performed below $E_\mathrm{C}(z)$, as electrons with higher energy are located inside the conduction band and are no longer tunnelling. At the interface, the integral should thus be computed up to $E_{\mathrm{C,max}}$, larger energies being already included in $J_{\mathrm{thermionic}}$. The value of the lower bound E_{min} depends on the shape of the barrier, and corresponds to the largest energy between

- the lower value of the conduction band at the interface $E_{\mathrm{C,min}}$ (as electrons must be in the conduction band);
- the value of E_C far from the interface on the side of the spike $E_{\mathrm{C},\infty}$ (as electrons with lower energy face a barrier with infinite thickness and thus cannot tunnel through it).

The transmission coefficient of charge carriers crossing a potential barrier is expressed using the one-dimensional WKB approximation, following [20]:

$$\mathcal{T}_{\mathrm{tunnel}}(E) = \exp\left(-\frac{2}{\hbar}\int_0^{z(E)} \sqrt{2m_{n,t}^*(E_\mathrm{C}(z') - E)}dz'\right). \qquad \text{(S7)}$$

$m_{n,t}^*$ corresponds to the effective mass of electrons in the layer in which they tunnel, and $z(E)$ is the first position in this layer where $E_\mathrm{C}(z) = E$, as represented in Figure S2. The transmission coefficient at a given energy E logically depends on the shape of the conduction band between 0 and $z(E)$, i.e. above E. When $E_{\mathrm{min}} = E_{\mathrm{C},\infty}$ - as represented in Figure S2 - the lower bound corresponds to the asymptotic value

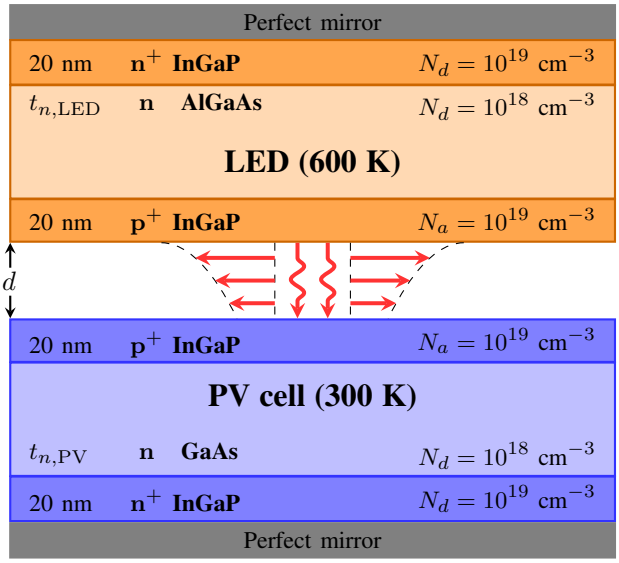

Fig. S3: Simple heterostructure-based AlGaAs/InGaP TPX device used for comparison with SCAPS.

of E_C and $z(E)$ can become large, making the integral over z time-consuming. Since the transmission coefficient goes to zero as E approaches $E_{C,\infty}$, the integral over depth is cut at an arbitrary distance z_c from the interface, which means that integration only starts at $E_{min} = E_C(z_c)$. The results presented in the main paper had been obtained setting this distance to 50 nm, which allows practically including the complete tunnelling contribution. Also, if the layer in which carriers tunnel is thinner than $z(E_{min})$, the integral is cut at the thickness of the layer, and reflection and transmission at this second interface are neglected.

The integration over energy for computing tunnelling current is simpler than in case of thermionic emission. Indeed, the condition of conservation of the momentum parallel to the interface no longer holds as the kinetic energy of tunnelling charges is not properly defined in the barriers. Therefore, only one integral over energy remains, and the current density of tunnelling electrons at a distance z from the interface is expressed as:

$$J_{n,\text{tunnel}}(z) = AT^2\varphi_n(z)e^{-\tilde{E}_{C,\max}}(\Phi_n^+ - \Phi_n^-), \qquad \text{(S8)}$$

where $\varphi_n(z)$, defined for z between 0^+ and $z(\tilde{E}_{min})$, is

$$\varphi_n(z) = \frac{m^*_{E_{C,min}}}{m_0}\int_{\tilde{E}_{min}}^{\tilde{E}_C(z)} e^{\tilde{E}_{C,\max}-\tilde{E}}\mathcal{T}(\tilde{E})d\tilde{E}. \qquad \text{(S9)}$$

Since the way we define the energy of charge carriers is not valid in the barrier, we consider that this expression can only be derived in the layer where $E_{C,min}$ is located: this is why $m^*_{E_{C,min}}$ appear in the above expression, as the final effective Richardson constant is then that of the aforementioned layer. The overall current density at the heterointerface can then be obtained by adding Eqs. (S5) and (S8) at $z = 0^+$, leading to Eq. (10) of the main paper (in which φ_n corresponds to $\varphi_n(0^+)$).

S.IV. Mesh size and computational time

The maximum power output returned by CRESCENT-1D along with the computational time are summarised in Table II for two sets of mesh sizes. Meshes are made from the concatenation of linear meshes, obtained either in each layer for z, in each frequency range above and below bandgap frequencies for ω, or for each radiative mode (propagating, frustrated, surface) for k_ρ. In the electrical solver, the spatial mesh is slightly modified to improve convergence at heterointerfaces. If 0 and t are the positions of the two boundaries of the layer, the spatial mesh includes these two positions and is linear between δz and $t - \delta z$, with δz being small (1 pm in the calculations presented in the article). This allows to compute precisely the derivatives at the interfaces.

When two mesh sizes are given for a parameter, they are respectively associated to the LED and the PV cell. CPU time is much greater than wall-clock time due to the simultaneous use of several processing cores.

TABLE II: Result and computational time obtained using two different sets of mesh sizes.

Section	Parameter		Low res.	High res.
Rad.	Mesh size	z	(301,201)	(401,301)
		ω	31	201
		k_ρ	60	300
	Comp. time	Wall-clock	50 s	30 min
		CPU	2 min 19 s	1h30
Elec.	Mesh size	z	(1801,1401)	(7001,6001)
		U	(25,25)	(121,121)
	Comp. time	Wall-clock	1 min 35 s	1h07
		CPU	4 min 52 s	3h18
Total	Comp. time	Wall-clock	2 min 25 s	1h37
		CPU	7 min 11 s	4h48
	Result	P_{max}	1.53 W.cm^{-2}	1.63 W.cm^{-2}

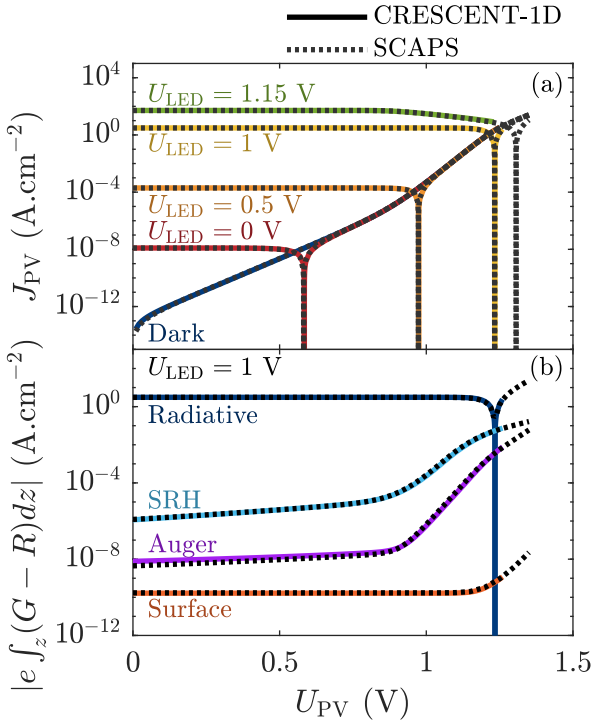

Fig. S4: Comparison of the drift-diffusion results obtained for the PV cell, compared to SCAPS.

S.V. Comparison with SCAPS

To compare CRESCENT-1D with SCAPS [21], we consider the heterostructure shown in Figure S3. The LED and the PV cell are supposed to have the same composition for simplicity, the device being not optimised for TPX operation. Since SCAPS cannot take a negative generation rate as an input, we cannot compare results relative to the LED: still, studying the PV cell is sufficient to ensure the solver works as expected. In this section, the iterative process on the chemical potential is not applied to make the analysis easier. The radiative quantities must be fed to SCAPS to allow for comparison, and are computed from our radiative solver. The generation rate can directly be used in SCAPS; to take the near-field electroluminescent emission of the PV cell into account, the radiative recombination coefficient B is directly computed from the photon emission rate as $B = \dot{N}_{em}(U = 0)/(n_i^2 t_{PV})$.

The PV cell I-V characteristic is provided in panel (a) of Figure S4 for different LED voltages. The results from our

solver and from SCAPS match well for any of the LED voltage considered, even for $U_{\mathrm{LED}} = 1.15$ V where J_{PV} slowly decreases before reaching U_{oc}. Due to the large current flowing through the device under such illumination, thermionic emission and charge carrier tunnelling have a considerable impact on the charge transport, and the match of I-V characteristics can therefore give confidence in the implementation of these phenomena. For $U_{\mathrm{LED}} = 1.15$ V however, CRESCENT-1D was not capable of converging close to U_{oc} precisely because of the large currents and of the different phenomena occurring. Nevertheless, this is not a significant issue for TPX devices as the PV cell performance is already too low at such voltages to allow efficient TPX operation.

For a more detailed comparison, the variation of the different PV cell generation and recombination rates with PV cell voltage are represented in panel (b) of Figure S4, considering an illumination obtained for $U_{\mathrm{LED}} = 1$ V. The match with SCAPS results is almost perfect for all voltages and all phenomena except for Auger recombinations at low voltage, whose rate obtained by our solver is slightly larger than the one returned by SCAPS - the ratio being almost equal to 2 for $U_{PV} = 0$ V. Under such low biases, Auger recombinations are mostly present in the intermediate layer and close to the interface. Since the charge carrier densities and currents vary rapidly there, the Auger recombination rate is highly sensitive to small differences present between solvers (spatial grid, numerical scheme, etc.), which can cause the observed difference.

REFERENCES

[1] J.-P. Mulet, "Modélisation du rayonnement thermique par une approche électromagnétique," Ph.D. dissertation, 2004.

[2] M. Francoeur, M. Pinar Mengüç, and R. Vaillon, "Solution of near-field thermal radiation in one-dimensional layered media using dyadic Green's functions and the scattering matrix method," *Journal of Quantitative Spectroscopy and Radiative Transfer*, vol. 110, no. 18, pp. 2002–2018, Dec. 2009.

[3] P.-O. Chapuis, S. Volz, C. Henkel, K. Joulain, and J. J. Greffet, "Effects of spatial dispersion in near-field radiative heat transfer between two parallel metallic surfaces," *Physical Review B*, vol. 77, no. 3, pp. 1–9, 2008.

[4] K. Joulain, "Near-field heat transfer: A radiative interpretation of thermal conduction," *Journal of Quantitative Spectroscopy and Radiative Transfer*, vol. 109, no. 2, pp. 294–304, Jan. 2008.

[5] H. Salihoglu, V. Iyer, T. Taniguchi, K. Watanabe, P. D. Ye, and X. Xu, "Energy Transport by Radiation in Hyperbolic Material Comparable to Conduction," *Advanced Functional Materials*, vol. 30, no. 6, p. 1905830, Feb. 2020.

[6] M. Schubert, J. A. Woollam, G. Leibiger, B. Rheinländer, I. Pietzonka, T. Saß, and V. Gottschalch, "Isotropic dielectric functions of highly disordered AlxGa1-xInP ($0\le x\le 1$) lattice matched to GaAs," *Journal of Applied Physics*, vol. 86, no. 4, pp. 2025–2033, Aug. 1999.

[7] M. A. Steiner, J. F. Geisz, D. J. Friedman, W. J. Olavarria, A. Duda, and T. E. Moriarty, "Temperature-dependent measurements of an inverted metamorphic multijunction (IMM) solar cell," in *2011 37th IEEE Photovoltaic Specialists Conference*, no. July. IEEE, Jun. 2011, pp. 002 527–002 532.

[8] M. Levinshtein, S. Rumyantsev, and M. Shur, *Handbook Series on Semiconductor Parameters, Vol. 2—Ternary and Quaternary III-V Compounds*. World Scientific, Nov. 1999.

[9] K. Alberi, B. Fluegel, M. A. Steiner, R. M. France, W. J. Olavarria, and A. Mascarenhas, "Direct-indirect crossover in GaxIn1-xP alloys," *Journal of Applied Physics*, vol. 110, no. 11, pp. 1–6, Dec. 2011.

[10] S. Adachi, *GaAs and Related Materials*. WORLD SCIENTIFIC, Oct. 1994.

[11] ——, *Optical Constants of Crystalline and Amorphous Semiconductors*. Boston, MA: Springer US, 1999.

[12] R. Ferrini, G. Guizzetti, M. Patrini, A. Parisini, L. Tarricone, and B. Valenti, "Optical functions of InGaP/GaAs epitaxial layers from 0.01 to 5.5 eV," *The European Physical Journal B - Condensed Matter*, vol. 27, no. 4, pp. 449–458, Jun. 2002.

[13] J. A. Gonzalez-Cuevas, T. F. Refaat, M. N. Abedin, and H. E. Elsayed-Ali, "Calculations of the temperature and alloy composition effects on the optical properties of AlxGa1-xAsySb1-y and GaxIn1-xAsySb1-y in the spectral range 0.5–6 eV," *Journal of Applied Physics*, vol. 102, no. 1, p. 014504, Jul. 2007.

[14] M. Sotoodeh, A. H. Khalid, and A. A. Rezazadeh, "Empirical low-field mobility model for III–V compounds applicable in device simulation codes," *Journal of Applied Physics*, vol. 87, no. 6, pp. 2890–2900, Mar. 2000.

[15] T. Sadi, I. Radevici, P. Kivisaari, and J. Oksanen, "Electroluminescent Cooling in III–V Intracavity Diodes: Efficiency Bottlenecks," *IEEE Transactions on Electron Devices*, vol. 66, no. 6, pp. 2651–2656, Jun. 2019.

[16] J. Legendre, "Theoretical and numerical analysis of near-field thermophotonic energy harvesters," Ph.D. dissertation, INSA Lyon, 2023.

[17] C. Wu and E. Yang, "Carrier transport across heterojunction interfaces," *Solid-State Electronics*, vol. 22, no. 3, pp. 241–248, Mar. 1979.

[18] A. A. Grinberg and S. Luryi, "On electron transport across interfaces connecting materials with different effective masses," *IEEE Transactions on Electron Devices*, vol. 45, no. 7, pp. 1561–1568, Jul. 1998.

[19] J. Verschraegen and M. Burgelman, "Numerical modeling of intra-band tunneling for heterojunction solar cells in scaps," *Thin Solid Films*, vol. 515, no. 15, pp. 6276–6279, May 2007.

[20] K. Yang, J. R. East, and G. I. Haddad, "Numerical modeling of abrupt heterojunctions using a thermionic-field emission boundary condition," *Solid-State Electronics*, vol. 36, no. 3, pp. 321–330, Mar. 1993.

[21] M. Burgelman, P. Nollet, and S. Degrave, "Modelling polycrystalline semiconductor solar cells," *Thin Solid Films*, vol. 361–362, pp. 527–532, Feb. 2000.